

THESIS FOR THE DEGREE OF LICENTIATE OF ENGINEERING

Sea Ice Concentration Estimation and Ice Type
Classification from Dual-Frequency Satellite Synthetic
Aperture Radar

WIEBKE ALDENHOFF

Department of Space, Earth and Environment
Division of Microwave and Optical Remote Sensing
CHALMERS UNIVERSITY OF TECHNOLOGY

Gothenburg, Sweden 2017

Sea Ice Concentration Estimation and Ice Type Classification from Dual-Frequency
Satellite Synthetic Aperture Radar
WIEBKE ALDENHOFF

© WIEBKE ALDENHOFF, 2017

Department of Space, Earth and Environment
Division of Microwave and Optical Remote Sensing
Chalmers University of Technology
SE-412 96 Gothenburg
Sweden
Telephone: +46 (0)31-772 1000

Cover:

Sentinel-1 C-band SAR image of sea ice in Fram Strait overlayed with results from
ice-water classification (22.10.2015).

Chalmers Reproservice
Gothenburg, Sweden 2017

Sea Ice Concentration Estimation and Ice Type Classification from Dual-Frequency Satellite Synthetic Aperture Radar

WIEBKE ALDENHOFF

Department of Space, Earth and Environment

Chalmers University of Technology

Abstract

The sea ice cover in the Arctic has undergone dramatic changes in recent years. The perennial sea ice extent is decreasing by 12.2 % per decade while annual mean sea ice thickness has decreased by more than 2 m for the central Arctic Basin from 1975 to 2012. High resolution information of the ice cover is necessary for a better understanding of the involved processes. Furthermore increased economic, scientific and touristic activities in the Arctic demand ice information for safer navigation in ice infested waters.

Satellite synthetic aperture radar facilitates year round monitoring of the sea ice cover with high spatial and temporal coverage. High resolution is a requirement to capture small scale sea ice features like leads and the dynamics of the ice cover driven by the atmosphere and ocean.

This thesis presents investigations on sea ice characterization from multi-spectral SAR imagery. Dual-polarization C- and L-band images from Sentinel-1 and ALOS PALSAR-2 have been used to derive sea ice concentration, for creation of ice-water maps and ice type classification.

The developed algorithms for sea ice concentration estimation and ice/water classification use spatial autocorrelation as a texture feature to improve the discrimination of ice and water. The mapping between image features and the output variable is realized with a neural network. The proposed algorithms show good performance when evaluated against manually derived ice charts and radiometer data. We demonstrate that C- and L-band contain complementary data and a combination of these frequencies could achieve more robust classification results.

Furthermore the separability and signatures of ice types in different ice regimes, i.e. marginal ice zone, pack ice and areas containing fast ice, have been investigated. Classification only based on backscatter intensities has been carried out by means of a support vector machine on selected examples of the same C- and L-band dataset. The results indicate that also for ice type classification a combination of frequencies can improve the classification accuracy.

Keywords: sea ice, SAR imaging, sea ice concentration, sea ice classification, Fram Strait

Acknowledgements

This thesis would not have been possible without my main supervisor Leif Eriksson and my examiner Lars Ulander, who gave me the opportunity for this research and are always helpful with discussions and comments about my work. Thanks to my assistant supervisor Céline Heuzé for pushing me the last few months and her rapid responses.

Coming to work is a pleasure thanks to my present and former colleagues at the Radar Group: Albert, Anders, Anis, Erik, Gisela, Jan, Lars, Maciej, Monika and Yufang. The rest of the department contributes to the nice atmosphere not only at break times and there is always help if you need it.

Last but not least big thanks to my friends and family, who are always there for a chat and a laugh and if you want to give your mind a rest.

Research contributions

This thesis is based on the work contained in the following papers:

- Paper A** W. Aldenhoff, A. Berg, and L. E. B. Eriksson. Sea ice concentration estimation from Sentinel-1 Synthetic Aperture Radar images over the Fram Strait. *2016 IEEE International Geoscience and Remote Sensing Symposium (IGARSS)*. IEEE, 2016, pp. 7675–7677. DOI: [10.1109/igarss.2016.7731001](https://doi.org/10.1109/igarss.2016.7731001)
- Paper B** W. Aldenhoff, C. Heuzé, and L. E. B. Eriksson. Comparison of ice/water classification in Fram Strait from C- and L-band SAR imagery. *Annals of Glaciology* (submitted)
- Paper C** W. Aldenhoff. *Information Content of Multi-spectral SAR data – Sea Ice Classification - Test Case Fram Strait*. Tech. rep. Chalmers University of Technology, 2017

Contents

Abstract	i
Acknowledgements	iii
Research contributions	v
1 Introduction	1
2 Synthetic Aperture Radar Principles	5
2.1 Radar Equation and Range Determination	5
2.2 Synthetic Aperture Radar	7
2.3 Radar Backscatter	10
3 SAR Imaging of Sea Ice	13
3.1 SAR Signatures of Sea Ice and Open Water	13
3.2 Texture Features for Image Classification	15
3.3 SAR Imagery of Different Frequency and Polarization	16
4 Sea Ice Characterization	19
4.1 Sea Ice Concentration	19
4.2 Sea Ice Classification	20
4.3 Sea Ice Motion	22
5 Summary of Appended Papers	25
5.1 Paper A: Sea ice concentration estimation from Sentinel-1 Synthetic Aperture Radar images over Fram Strait	25
5.2 Paper B: Comparison of ice/water classification in Fram Strait from C- and L-band SAR imagery	25
5.3 Paper C: Information Content of Multi-Spectral SAR	26
6 Conclusions and Outlook	29
Bibliography	31
Paper A	39
Paper B	45
Paper C	63

1 Introduction

Sea ice is covering the central part of the Arctic Ocean all year round and has long been a natural barrier for exploration and exploitation of the far north (see Figure 1.1). Though the extent of the sea ice cover has a large natural variability from year to year, long term trends show a decline in extent of approximately 12.2 % per decade since 1980 [1] as well as a reduction of annual mean ice thickness by 0.58 m per decade in the Arctic Basin [2].

The retreat and thinning of the ice is not only a threat for the pristine and vulnerable environment with its unique fauna and flora, but also one of the most visible signs of climate change. Sea ice acts as an insulator between the ocean and the atmosphere and a change in the sea ice cover impacts the heat balance of the Arctic and thus the climate system in the whole region [3]. Monitoring the state of the sea ice is therefore crucial to our understanding of climate changes and the processes involved.

The retreating ice also induces an improved accessibility of the Arctic which already leads to extended scientific, economic and touristic activities in this region. The traffic volume is increasing in the Arctic, but still dependent on the ice situation [4]. Safe navigation in ice-infested waters demands accurate, detailed and timely information about the sea ice conditions to minimize the risk of accidents and to protect the environment.

Systematic monitoring of the Arctic sea ice cover has long been hampered by the harsh and cold environment. Regular observations of the sea ice extent started with hunting and whaling activities in the mid 19th century. Though not primarily made for scientific purposes they are a valuable source of historical sea ice data [5]. Those observations were limited to the sea ice edge as shipping technology did not permit to travel further into the ice. The first noticeable attempt to describe sea ice scientifically was within the scope of the Austro-Hungarian Arctic Expedition led by Payer and Weyprecht 1872-1884 [6]. The voyage of the Fram lead by Fridtjof Nansen 1893-1896 was a great step forward in understanding the oceanography, geography and ice cover of the Arctic [7]. Development of airship technology facilitated airborne remote sensing observations of the Arctic in the late 1930s of last century [8]. The development continued from airborne to spaceborne observations made with satellites which founded an era of continuous and large scale measurements of the ice cover. Since 1978 a consistent dataset of sea ice concentration exists from passive microwave radiometer measurements [9]. Despite

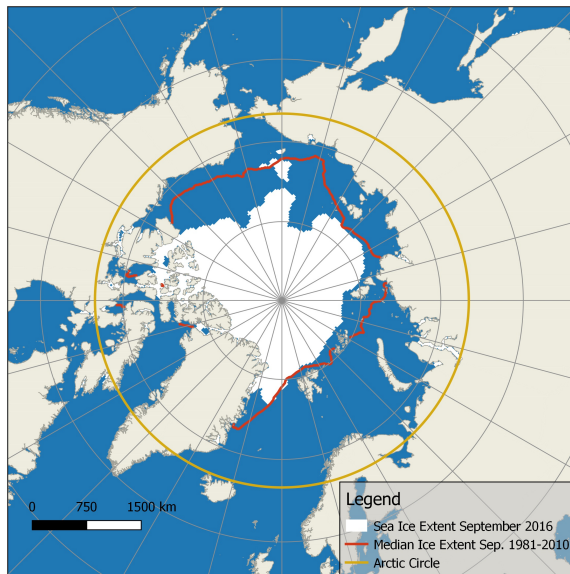


Figure 1.1: *Map of the Arctic (Ice extent from NSIDC)*

the progress in remote sensing data, in-situ measurements of sea ice parameters remain scarce in space and time.

Remote sensing of the sea ice cover comprises several different techniques operating in a wide range of frequencies in the electromagnetic spectrum. Optical remote sensing, encompassing the visible part of the electromagnetic spectrum with wavelengths in the range 390–700 nm, is widely used as images are straightforward to interpret for the human visual system. Observations are limited to the polar summer seasons due to lack of sunlight during polar night and are obstructed by cloud coverage. Measurements in the infrared region, wavelengths in the range 0.75–1000 μm , exploit temperature differences between different surface types but are also largely affected by cloud layers. These limitations are overcome by microwave remote sensing with wavelengths in the range of 0.01 m to 1 m. The atmosphere is almost transparent in this frequency range, except for some narrow absorption bands of atmospheric gases, and the radiation is not significantly affected by clouds, haze and all but the heaviest rain. This is due to longer wavelengths in the microwave region which are not susceptible to atmospheric scattering. Observations, either passive (only receiving) or active (transmitting and receiving), can be made all year round and thus cover the whole seasonal cycle. These advantages make microwave remote sensing the number one choice for consistent monitoring the sea ice cover.

Depending on the task at hand different microwave remote sensing techniques are used for sea ice observations. Passive microwave radiometry is employed for sea ice

concentration and area/extent measurements as well as first year and multi year ice concentrations [10, 11]. Radar, an active remote sensing sensor, is used in different techniques. Sea ice thickness can be estimated from altimetry data [12], while synthetic aperture radar (SAR) imagery can be used for sea ice drift estimation [13], ice classification and determination of area/extent [14, 15]. SAR imagery of sea ice is usually obtained from airborne and spaceborne sensors. Airborne measurements offer high resolution at the expense of spatial coverage and are often used for campaigns or reconnaissance focused on smaller areas. Spaceborne measurements have a large spatial and temporal coverage with moderate to high resolutions and are used for monitoring and operational purposes.

Automated image classification of sea ice and distinction of ice and water is not a straightforward task. The backscatter intensity of sea ice encompasses a wide range of values and depends on the properties of the ice, e.g. surface roughness, snow layer, dielectric properties, as well as on the parameters of the radar system, e.g. frequency, polarization, incidence angle. Radar is most sensitive to the properties of the surface and upper layer of the ice which undergoes changes with time and also depend on the ambient conditions, e.g. wind, precipitation, temperature. While a smooth water surface has a very low backscatter intensity, wind roughening can increase the backscatter of water to cover the range of typical backscatter values of ice [16]. Hence for robust classification of ice types and the distinction of ice from water spectral, contextual, textural as well as temporal information are necessary and need to be extracted from the images.

The focus of our studies is Fram Strait, located between Svalbard and Greenland. This area is of special interest as it's sea ice cover is highly dynamic and different ice regimes, i.e. fast ice, first year ice, multi year ice as well as the marginal ice zone, are present. This imposes high demands on temporal and spatial resolution to capture the ever changing environment. The majority of sea ice exported from the Arctic is transported through Fram Strait and this area thus plays an important role in the sea ice mass balance of the Arctic [17].

The idea behind the work presented in this thesis is the question of whether the use of multiple frequencies can improve the accuracy of automatic image analysis for sea ice parameter retrieval with high spatial and temporal resolution. Therefore an algorithm, using texture features and backscatter intensities, has been developed for automatic estimation of sea ice concentration and ice/water classification from dual-polarized SAR imagery of present spaceborne sensors, i.e Sentinel-1 in C-band (about 5 cm wavelength) and ALOS PALSAR-2 in L-band (about 20 cm wavelength). The use of neural networks for mapping image features into sea ice parameters allows for easy inclusion of more features and once trained it can be applied to an unknown image. The algorithm performance is validated against ice charts and radiometer data and showed good results. Comparison of the two frequencies revealed potential that a combination could assist in retrieving more robust estimates.

Furthermore separability and signatures of ice types in different ice regimes, i.e. marginal ice zone, pack ice and areas containing fast ice, have been investigated. A support vector machine with backscatter intensities as input has been used

for classification of selected C- and L-band image pairs. Once more the different imaging properties of the two frequencies underline the potential benefit of multi-spectral analysis. Future work should concentrate on the limitation posed by the constant movement of sea ice, which impacts the co-registration of images of different frequencies.

The thesis is structured the following way: at first an introduction to principles of synthetic aperture radar is given to impart the unfamiliar reader with the necessary foundation to follow the rest of the thesis. The following chapter presents a more thorough discussion of backscatter from sea ice and open water as well as concepts and challenges of automatic analysis of sea ice imagery. The thesis concludes with a brief summary of the appended papers and conclusions and outlook into future research activities.

2 Synthetic Aperture Radar Principles

The term radar, short for **R**adio **D**etection **A**nd **R**anging, embraces techniques that use electro-magnetic radiation in a broad range of frequencies from 3 MHz to 100 GHZ for remote sensing purposes or non-destructive testing [18]. Initially invented for military applications, radars are nowadays widely used for many different civilian applications including parking assistance in vehicles, velocity measurements of cars, weather (rain) radar as well as ship- and air-traffic surveillance. Radar imaging refers to a 2- or 3-dimensional map of backscatter intensities created from the transmitted signal.

Radars are active devices that transmit an electro-magnetic signal and receive the reflected echoes. Thus they are independent of external illumination sources and can be operated whenever needed. The choice of frequency depends on the application and the focus of this thesis is in the microwave region. Typical radar frequencies used for imaging and their nomenclature are shown in Table 2.1.

Earth's atmosphere is almost transparent for frequencies in the microwave region and these frequencies are unaffected by clouds due to their comparatively large wavelength [20]. These properties make satellite radar remote sensing a good choice for large scale and continuous monitoring of the Earth's surface.

2.1 Radar Equation and Range Determination

The power of the received reflected or backscattered signal can be described by the radar equation. For the monostatic case, that is the same antenna is used for transmission and reception, the radar equation is given by [21]

$$P_r = P_t \cdot \frac{\sigma \lambda^2 G^2}{(4\pi)^3 R^4 L}, \quad (2.1)$$

Table 2.1: Commonly used radar frequencies and nomenclature [19]

Band name	Frequency	Wavelength
L	1–2 GHz	15–30 cm
C	4–8 GHz	3.75–7.5 cm
X	8–12 GHz	2.5–3.75 cm

where $P_{r,t}$ are the received and transmitted power, G the antenna gain, λ the wavelength, L accounts for losses, R is the range to the target and σ the radar cross section (RCS) of the scattering object.

The RCS describes the ability of a target to reflect the incident energy back to the radar. The RCS depends on the physical properties of the reflecting object, e.g. shape, size and material, and the frequency and polarization of the incident radiation.

For distributed targets, i.e. large surfaces, the backscatter coefficient σ^0 is defined by

$$\sigma^0 = \left\langle \frac{\sigma_i}{A} \right\rangle, \quad (2.2)$$

where $\langle \rangle$ means averaging, A the surface area of a resolution cell and σ_i the RCS of individual scatterers. It is used to characterize the backscattered signal [22]. σ^0 depends on the incidence angle and an alternative parameter which reduces this dependency is the quantity γ^0

$$\gamma^0 = \frac{\sigma^0}{\cos \theta_i} \quad (2.3)$$

where θ_i is the incidence angle [23].

2.1.1 Range Resolution

The range R from the radar to a target is determined by measuring the travel time t between transmission and reception of the signal:

$$R = \frac{c \cdot t}{2} \quad (2.4)$$

where c is the propagation speed and the factor 2 accounts for the two-way delay.

Range resolution is the ability of the radar to discern nearby targets in the range direction. For a simple monochromatic and unmodulated pulse the range resolution is defined as follows [24]:

$$\Delta R = \frac{c \cdot \tau}{2} \quad (2.5)$$

where τ is the pulse length. The shorter the pulse length the better the range resolution will be. To maintain the signal-to-noise ratio (SNR) as pulses get shorter, higher pulse powers are needed and thus raise the demands on the hardware. Therefore unmodulated pulsed radars are limited in their range resolution capabilities.

To overcome these limitations, linear frequency modulated pulses are widely used in modern radars. The range resolution of such a waveform is defined by [21]

$$\Delta R = \frac{c}{2 \cdot B} \quad (2.6)$$

where B is the bandwidth of the waveform. In this way longer pulses can be used to increase the SNR and still a good range resolution can be achieved.

2.1.2 Azimuth Resolution

2- and 3-dimensional imaging can be achieved by sweeping the antenna over the desired area or volume. The resolution is determined by the size of the antenna footprint, i.e. the size of the area illuminated by the radar, in the targeted area (see Figure 2.1). The beamwidth of an antenna of size D with $D \gg \lambda$, the wavelength of the transmitted signal, is approximately

$$\Delta\beta \approx \frac{\lambda}{D} \quad (2.7)$$

and the footprint size at a certain range R is thus given by

$$\delta x = \Delta\beta \cdot R \approx \frac{\lambda \cdot R}{D}. \quad (2.8)$$

The resolution depends on the range and the size of the antenna; the larger the antenna and shorter the range the better the resolution will be. For spaceborne systems with large ranges between the target and the antenna, this means very large antennas would be needed to achieve a good spatial resolution.

2.2 Synthetic Aperture Radar

High resolution imaging with conventional or real aperture radar systems, i.e. where the resolution is determined by the antenna size, is limited by the impracticability of large antennas. To overcome these limitations a technique called **Synthetic Aperture Radar (SAR)** is used, where a larger antenna is artificially created by moving a smaller antenna along a defined path.

The final image is not directly available and needs to be created by signal processing from the measured data. Many different algorithms for image formation have been invented to accommodate varying imaging scenarios and to reduce computational load for processing [25][26].

The imaging geometry of an air- or spaceborne SAR system is shown in Figure 2.1. The direction of the antennas flight path is called along track or azimuth direction. The range or across track direction is oriented perpendicular to the azimuth direction. Two different ranges are considered, firstly the slant range and secondly the ground range. The first one describes the direct distance from the antenna to the object while the second one refers to the projection of the slant range onto the ground plane. The radar is operated in a side-looking configuration (see Figure 2.2). The elevation or look angle is the angle between the nadir position of the radar and the slant range direction. The incidence angle is defined between the normal of the Earth's ellipsoid and the slant range direction. The local incidence angle takes the actual slope of the Earth's surface into account. The incidence angle for SAR imaging usually varies in the range 20–50°.

2.2.1 SAR Imaging Modes

Synthetic Aperture Radars can be operated in different imaging modes to accommodate various demands regarding resolution and spatial coverage of the imagery.

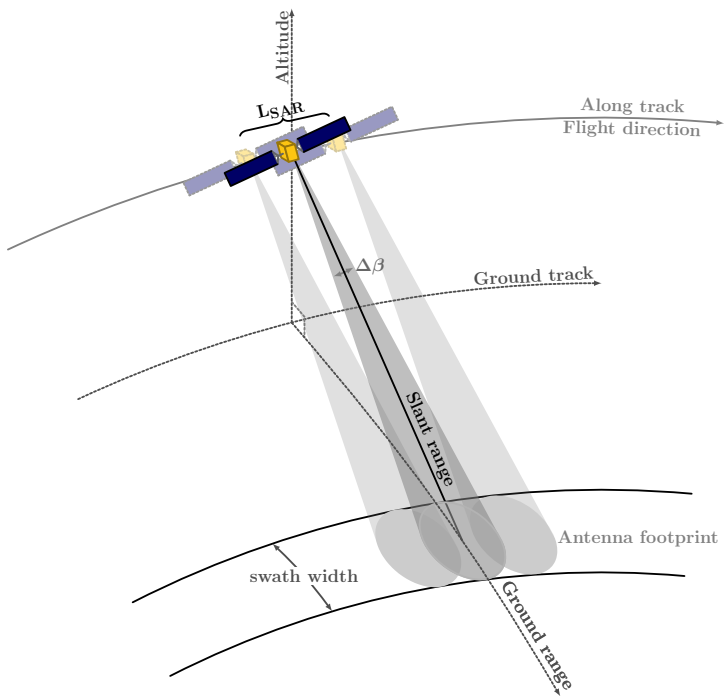


Figure 2.1: *SAR geometry*

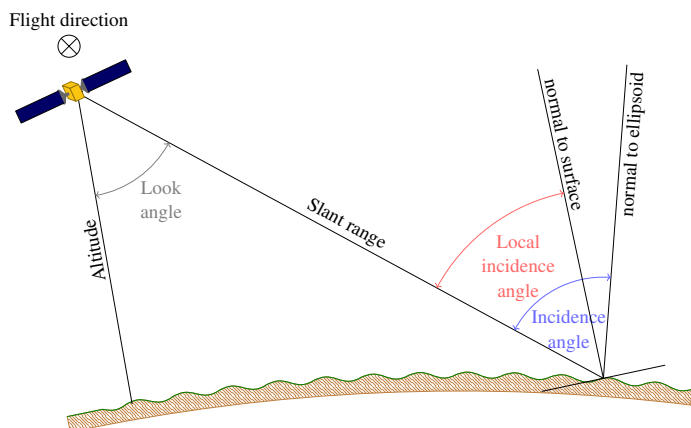


Figure 2.2: *Side-looking SAR with definition of angles*

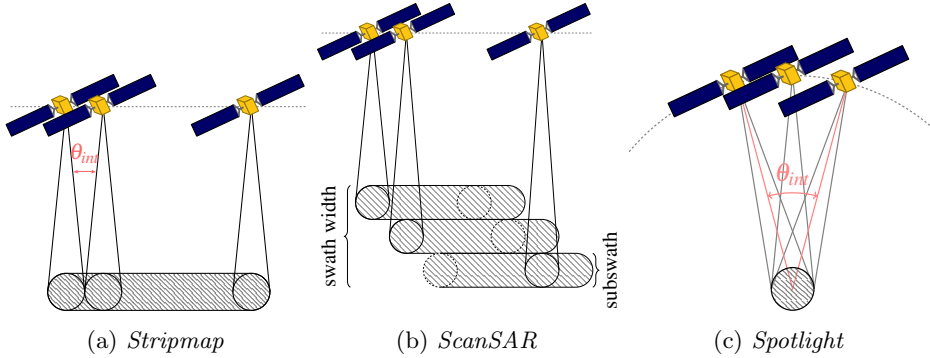


Figure 2.3: *Integration angles of different SAR modes*

The standard mode is the so called stripmap mode (see Figure 2.3a). The antenna is pointing at a fixed direction and the spatial coverage is limited in width by the footprint of the antenna on the ground.

Larger spatial coverage with swath widths up to several hundred kilometres can be achieved with ScanSAR (see Figure 2.3b). In this mode the antenna is steered to different locations in range, producing so called subswaths, which, stitched together, give the final wide swath image. Thus a larger area can be covered at the expense of resolution, which is usually around 100 m [27]. Another variant is TOPSAR, where the antenna is steered in azimuth and range to reduce image artefacts compared to traditional ScanSAR [28].

Spotlight mode SAR is the choice if a high spatial resolution is more important than coverage. In this mode the antenna is steered to observe a target area for a longer period of time (see Figure 2.3c). For spaceborne SARs resolutions less than a metre can be achieved [29].

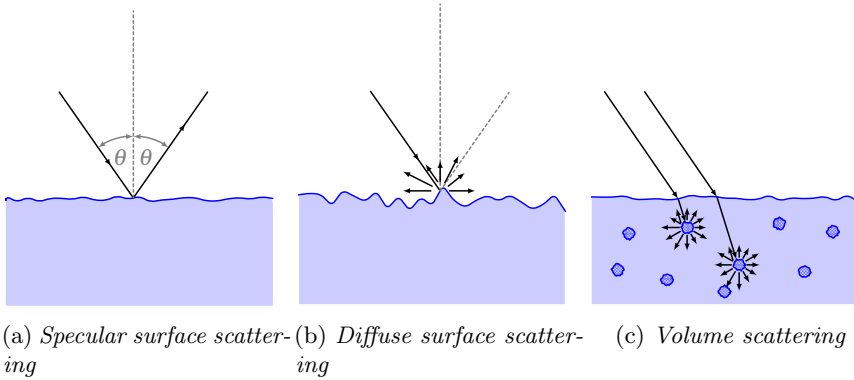
2.2.2 Resolution

The resolution in range is the same as for the real aperture radar and depends on the bandwidth of the signal waveform according to Equation 2.6. It should be noted here that the slant range resolution is independent of range while the ground range resolution increases with range due to the side-looking imaging geometry. The advantage of SAR imaging is the resolution in azimuth direction, which can be defined as follows:

$$\delta x = \frac{\lambda}{2\theta_{int}}, \quad (2.9)$$

where λ is the wavelength and θ_{int} the integration angle, i.e. the angular extent over which the scene of interest is sampled [22]. The integration angle depends on the imaging mode of the SAR system (see Figure 2.3).

For strip map collection in broadside geometry the integration angle is equivalent to the beam width of the real antenna (see Figure 2.3a). With the beam width

Figure 2.4: *Different scattering mechanisms*

from Equation 2.7 the azimuth resolution is

$$\delta x = \frac{\lambda}{2\frac{\lambda}{D}} = \frac{D}{2}, \quad (2.10)$$

where D is the size of the real antenna. The azimuth resolution of a SAR system is hence independent of the range to the target and the smaller the antenna the better the resolution will be. A lower bound of antenna size is imposed by the Signal-to-Noise ratio and range-Doppler ambiguities.

2.3 Radar Backscatter

The backscattered intensity mainly depends on the radar system parameters, e.g. frequency, polarization and incidence angle, and on the properties of the target, e.g. dielectric constant, geometrical shape and for distributed targets also on surface roughness and the homogeneity of the medium. Two different mechanisms are used to describe the scattering process: surface and volume scattering.

Surface scattering takes place at the interface of two homogeneous media, in the case of remote sensing these are usually air and the medium of interest (see Figure 2.4a and 2.4b). The scattering intensity is governed by the dielectric properties of the medium and the roughness of the surface. Whether a surface appears smooth or rough depends on the wavelength of the radar signal. A surface is defined as smooth if the Rayleigh criterion

$$\Delta h < \frac{\lambda}{8 \cos(\theta)} \quad (2.11)$$

where Δh is the standard deviation of surface height, λ the wavelength and θ the incidence angle, is fulfilled. The backscattered intensity increases with surface roughness. For a smooth surface specular reflection occurs and thus the backscattered intensity is negligible. Double or triple bounce at perpendicular surfaces also increases the backscattered signal.

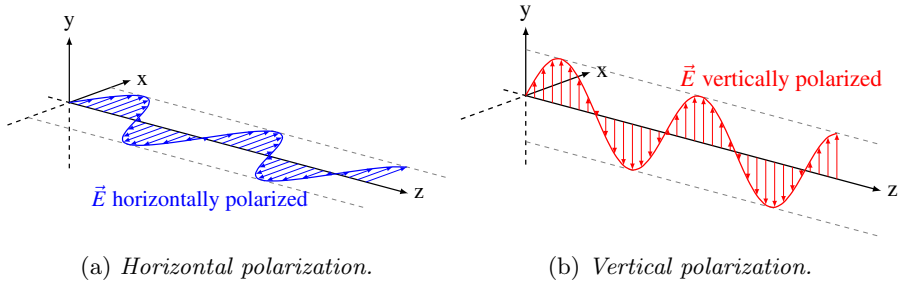


Figure 2.5: *Polarization states of transmitted wave*

Volume scattering occurs when the radar wave penetrates into a medium and is scattered by particles or dielectric inhomogeneities within the medium. A schematic sketch of volume scattering is shown in Figure 2.4c. The penetration depth is a measure for the distance a wave can penetrate into a medium and usually increases with decreasing frequency. The distribution and the size of the particles relative to the wavelength of the wave play an important role for the scattering within the medium.

Both scattering mechanisms usually occur at the same time, but depending on surface properties one can be negligible compared to the other. More detailed descriptions can be found in [23, 30].

The scattering process is also sensitive to the polarization of the incident wave. Polarization refers to the orientation of the electric field vector of a radar wave, where the field vector oscillates perpendicular to its propagation direction. Radars usually transmit and receive linearly polarized signals, e.g. the field vector is confined to one plane which is either horizontally (H) or vertically (V) oriented with respect to the propagation direction (see Figure 2.5). Scattering with multiple scattering events, e.g. volume scattering or extremely rough surfaces, can alter the polarization state of the radar wave; this process is known as depolarization [31]. Additional information about a target can thus be gained by using dual-polarized data, where both polarizations are received, or fully-polarimetric data, where both polarizations are transmitted and received. If the same polarization is transmitted and received the data is said to be co-polarized and the channel is denoted as either HH or VV; cross-polarization is used to define different polarizations on transmission and reception, which is abbreviated by HV or VH.

3 SAR Imaging of Sea Ice

Fundamental to the interpretation of sea ice SAR imagery is the understanding of the different factors influencing the backscatter intensities of sea ice and open water. The sea ice cover is undergoing constant changes driven by atmosphere and ocean changing its appearance in SAR imagery. Especially for wide swath imagery where a broad range of incidence angles and different ice and atmospheric regimes are covered in the same image, the backscatter intensities vary considerably. Radar backscatter of a surface is generally governed by

1. the dielectric properties of the material
2. surface roughness and inclusions of scattering inhomogeneities
3. frequency, polarization and sensor geometry of the radar.

The first two describe the physical properties of the surface and the latter one the characteristics of the imaging system. Radar scattering is most sensitive to the surface and upper layer of the scattering medium.

3.1 SAR Signatures of Sea Ice and Open Water

3.1.1 Radar Backscatter of Open Water

An incoming radar wave is reflected almost specularly by a calm ocean surface, resulting in a low backscatter intensity. However the ocean surface is seldom flat as wind introduces surface roughness originating from capillary and gravity waves. Backscatter intensities increase with the roughness (see also Section 2.3) of the surface and hence with wind speed [32]. The backscatter of a roughened ocean surface depends on the incidence angle and the orientation of the waves relative to the look direction of the radar for the co-polarization channel [33]. For the cross-polarization channel the backscatter is significantly lower, about 10 dB compared to co-polarization and below the noise floor of many spaceborne SARs, and almost independent of incidence angle and wind direction [34].

Depolarization is small because the high dielectric constant of sea water leads to primarily surface scattering and little penetration into the water. The cross-polarization channel therefore greatly enhances the ice water contrast in SAR imagery [35]. The left part of Figure 3.1 summarizes the scattering mechanism over open water.

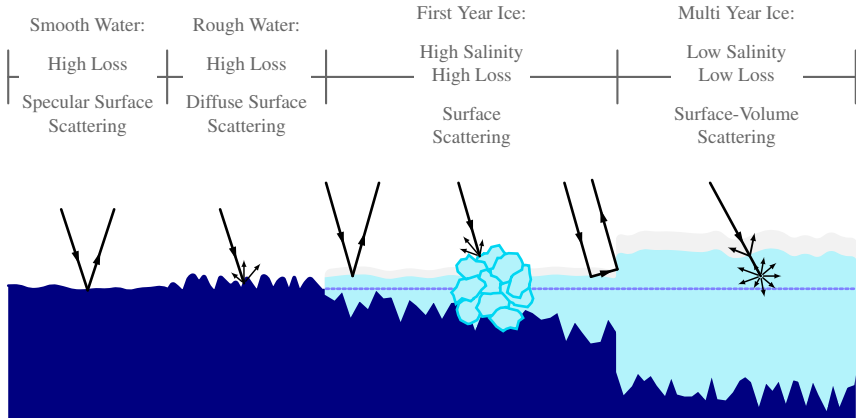


Figure 3.1: *Scattering mechanisms in ice and water. Adapted from [38, p. 74]*

The ocean in general is not a homogeneous surface and especially over wide swath imagery the surface roughness is varying over the image. The presence of biogenic or anthropogenic surface films can dampen the wind induced roughness and hence reduce backscatter even for high wind conditions [36]. Furthermore oceanic phenomena like upwelling/downwelling can modulate the sea surface roughness as well as atmospheric effects as boundary layer stability [32]. Close to land wind shadowing can reduce backscatter over the ocean surface [37].

3.1.2 Radar Backscatter of Sea Ice

Sea ice is an inhomogeneous mixture of freshwater ice, liquid brine inclusions and air pockets or bubbles. Its composition depends on the ambient conditions, e.g. wind, waves, temperature, when it was formed and its age, as weathering processes alter the state of the sea ice. Brine will be drained from the ice by gravity or expulsion over time resulting in a lower salinity of older ice. Furthermore the summer melt cycle facilitates crystal restructuring within the ice. The dielectric properties of sea ice are hence a complex function of the volume fraction of its constituents, the age of the ice and shape, size and orientation of the brine pockets and air bubbles, which are to a large extent controlled by the temperature of the ice [38][31]. The backscatter of first year ice is mostly characterized by surface scattering but multi year ice with its lower salinity facilitates volume scattering (see Figure 3.1).

Scattering is largely influenced by surface roughness. Small scale surface features in the order of the wavelength, like frost flowers, can greatly enhance the backscatter values over ice [39] [40]. Topographic features like ridges can also increase the backscatter intensities because of multi bounce or surfaces inclined towards the radar [41]. The surface of the ice can be covered with a layer of snow. While dry snow has little impact on the backscatter intensity, wet snow can reduce the backscatter intensity significantly and the backscatter intensity becomes more

frequency dependant [38]. Ambient conditions also influence the backscatter signatures of sea ice, as the temperature of the ice and the moisture content of the snow layer changes the dielectric properties [42]. Thus the radar signature is more attributed to its surface and upper layer properties, which might lead to complications to distinguish different ice types.

The backscatter intensity of sea ice depends on the frequency of the SAR system. For higher frequencies (C- and X-band) small scale surface features in the order of a few centimetres have a larger influence on the backscatter compared to lower frequencies like L-band. Furthermore volume scattering is more pronounced for the shorter wavelengths because of the size of the scattering inhomogeneities inside the ice [38]. Lower frequencies with their larger penetration depths are preferable under melting conditions, when they can penetrate through a wet snow cover, and for detection of deformation features [43][44]. Ice type classification and distinction of surface deformation features like ridges can be improved by considering the cross-polarization channel [45][46].

3.2 Texture Features for Image Classification

A robust automated classification scheme needs to be able to cover the large varieties of backscatter values of sea ice and open water. This is especially true for wide swath images mostly employed for monitoring purposes, where different ice regimes and ambient conditions are covered within a single image. Because of large variations and overlap of backscatter signatures of water and ice, backscatter alone is not sufficient for a robust classification [47].

Therefore tonal/spectral variations, textural and contextual features are taken into account. Texture describes the spatial variations of image brightness values within an image part while the contextual features cover the relation of the image part to its surrounding. While texture can be recognized and described empirically, i.e using adjectives like smooth, rough, irregular or rippled, relatively easily by humans, it is difficult to give a precise definition a computer can process [48]. In the course of time different texture features have been proposed and employed in sea ice classification schemes: gray level co-occurrence matrices, a second order texture feature[14][49][50], autocorrelation, which has been successfully employed in the Baltic [51][52], as well as Markov random fields [53].

Autocorrelation has been applied in the algorithms developed in the framework of this thesis. The normalized autocorrelation of an image block for lag (i, j) is defined as follows:

$$A(i, j) = \frac{1}{n - 1} \frac{\sum_{xy} (I(x - i, y - j) - \mu)(I(x, y) - \mu)}{\sigma^2} \quad (3.1)$$

where n is the number of pixels, μ the mean value and σ the standard deviation of an image block. Autocorrelation gives information about the coarseness of the texture and can detect repetitive patterns [54]. Over ice neighbouring pixels are assumed to be more related to each other while the backscatter values over open water fluctuate more randomly resulting in lower autocorrelation values.

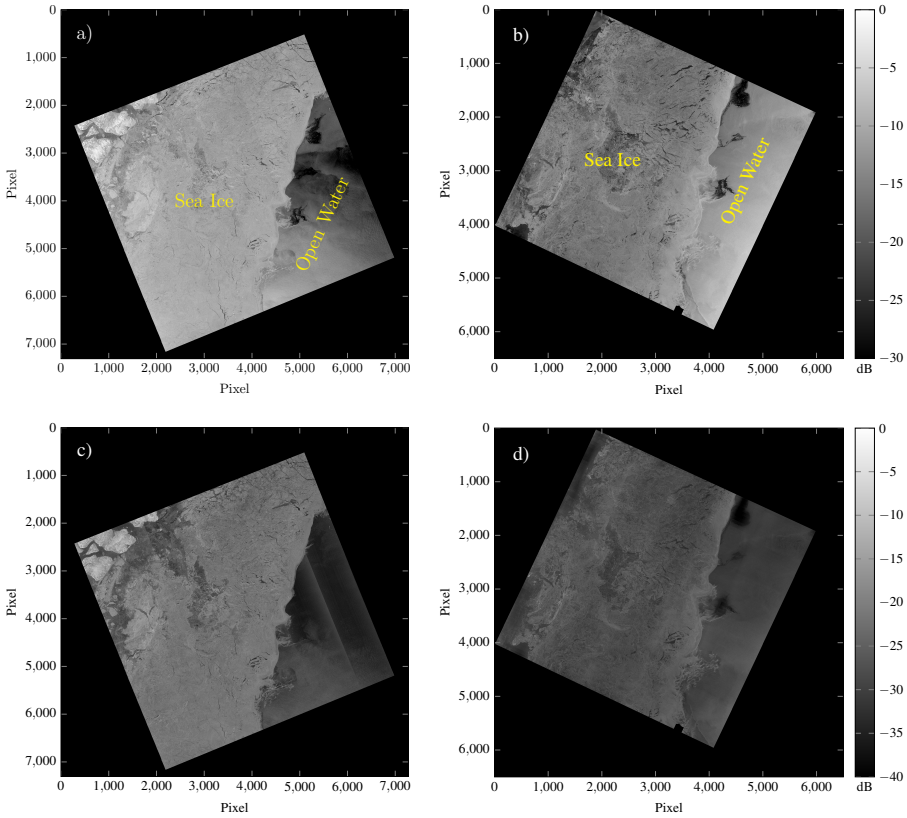


Figure 3.2: *SAR images of sea ice from 09.01.2016: a) C-band HH, b) L-band HH, c) C-band HV, d) L-band HV, where C-band imagery is from Sentinel-1 and L-band imagery from ALOS PALSAR 2 [Contains Copernicus Sentinel Data (2016)]*

Nevertheless some sea ice areas show little texture, e.g. smooth fast ice and areas in the MIZ where subresolution ice floes lead to a more random and smooth texture, while texture over open ocean can be introduced by wind patterns or oceanic features, e.g upwelling and eddies (see section 3.1.1).

Autocorrelation is computed for image blocks around the pixel of interest with lags in all directions and the average is assigned as the new pixel value. The size of the image block is important, as it needs to capture the prevalent texture features of the image. For our purposes a block size of 11x11 pixels has given the best results.

3.3 SAR Imagery of Different Frequency and Polarization

The primarily used frequency for operational sea ice observations and monitoring is C-band [55], providing a 25 year record of observations starting with ERS-1/2 in

1991/1995, RADARSAT 1/2 since 1995/2007, Envisat ASAR 2002 and the two Sentinel-1 satellites since 2014/2016. Studies have shown that other frequencies, X- and L-band in particular, can add complementary information that can facilitate interpretation and classification of SAR imagery [44, 56]. L-band, due to its larger wavelength, can aid to improve image interpretation during melting conditions compared to higher frequencies [57].

Dual polarization imagery (mostly HH and HV) is state of the art for image interpretation and is supported by most current spaceborne SAR missions. The cross polarization channel can help to improve the distinction of different ice types and ice/water discrimination [58]. Depolarization is related to volume scattering or multiple scattering processes associated with rough surfaces, and hence lower for water areas [31]. But care must be taken for the cross-polarization images when the backscatter reaches the noise floor. At these low backscatter values, noise floor variations especially at boundaries between subswaths can become visible and impede automatic classifications [59].

Figure 3.2 shows dual-polarization images from Sentinel-1 in C-band (5.405 GHz) and ALOS PALSAR 2 in L-band (1.2 GHz). Imagery from these two SAR systems has been used throughout the work contained in this thesis. The cross-polarization channel of the Sentinel-1 image in 3.2c) shows prominent striping over areas with low backscatter (right part of the image) due to noise floor corrections. Striping is not so pronounced for the PALSAR 2 image, although not evident in this image, reduced image quality has been observed for many low backscatter areas. The contrast between ice and water (right part of the image) is more pronounced in the cross-polarized channel of C-band compared to L-band.

4 Sea Ice Characterization

The sea ice cover can be described in more detail by properties derived from SAR imagery:

1. Sea Ice Concentration
2. Sea ice Classification: ice/water discrimination, ice types
3. Sea Ice motion

4.1 Sea Ice Concentration

Sea ice concentration is the areal fraction of sea ice covering the ocean surface in a predefined region. Sea ice concentration plays an important role for air-ice-sea interaction processes and is thus of interest to atmospheric studies and climate modelling [60]. Concentration information is also valuable for navigation in ice infested waters, as high concentration areas are usually to be avoided [61].

Ice concentration in ice charts issued by national ice services, is defined in tenths on a scale ranging from 0 = ice free to 10/10 = consolidated pack ice [62]. Percentage is also a widely used unit to describe ice concentration for instance datasets derived from passive microwave radiometry.

A continuous time series of ice concentration observations with a spatial resolution of 25x25 km exists for the Arctic and Antarctica from passive microwave radiometer data since 1978 [63]. Daily ice concentration maps are also issued by the University of Bremen based on AMSRE-2 data with a resolution down to 3.125 km [64]. The low resolution limits the use for navigational purposes but the data is widely-used in climatological studies. For navigation, National ice services provide ice information with higher spatial resolution. The charts are derived manually from a number of different data sources including optical, microwave and infrared remote sensing data as well as information from ships or reconnaissance missions [65]. When using ice charts as reference data it should be pointed out that they are biased towards the C-band data, which is the primary information source in the manual interpretation process.

Manually derived ice charts are a subjective interpretation of the expert ice analyst and thus depend on the experience level as well as on the person itself [66]. Furthermore manual interpretation is usually accompanied with generalization on

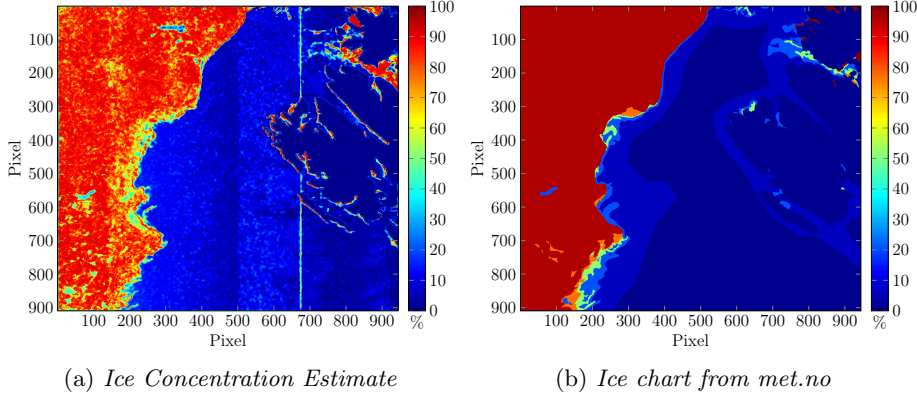


Figure 4.1: *Ice concentration from algorithm and ice chart [from Paper A]*

the expense of resolution. To overcome these limitations scientific efforts have been undertaken to automatize this process. Although the human brain can process complex imagery relatively easily and effectively, digital implementing is not a straightforward task [67]. To date manual interpretation has not been fully replaced by automatic evaluation procedures.

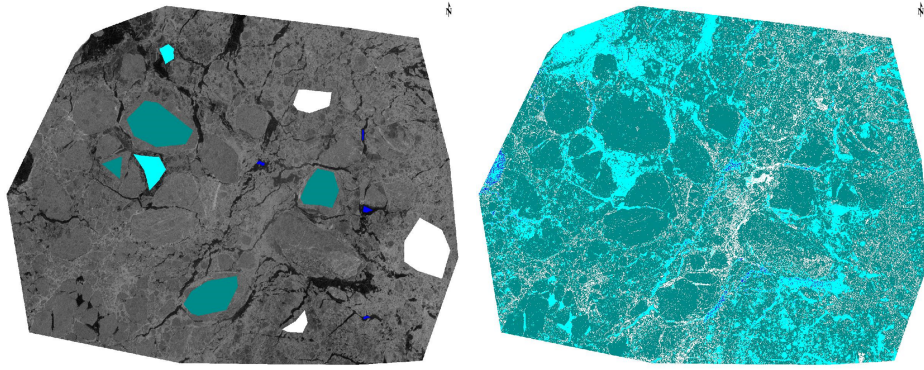
Sea ice concentration estimation from SAR imagery consists of feature extraction and mapping of the feature vector to ice concentration. Features include backscatter coefficients, polarization ratios and texture measures. Mapping is usually done with a machine learning approach or statistical classifiers.

Autocorrelation as texture feature and feedforward neural networks have been used on single and dual polarization data for sea ice concentration estimation in the Baltic [47, 51, 52]. Gray Level Co-occurrence matrices derived texture features in conjunction with a data assimilation process are exploited in an algorithm using RADARSAT-2 images in the Canadian Arctic [68]. An approach with automated feature learning only based on backscatter intensities is using a convolutional neural network, widely-used in other fields of computer recognition, for the mapping process [69]. A Bayesian approach is used to fuse ice-water maps from RADARSAT-2 imagery with ice concentration derived from AMSR-E to improve the concentration estimates. The only algorithm using L-band is based on scattering entropy of polarimetric data and simple thresholding [70].

Figure 4.1 shows an example of ice concentration derived from Sentinel-1 data with the algorithm presented in Paper A in comparison with an ice chart from met.no.

4.2 Sea Ice Classification

Sea ice classification aims to further characterize sea ice according to its type, stage of development, presence of ridges or melting state. Once again this is valuable information for navigation in ice infested waters and changes of the characteristics



(a) *L-band HH image from ALOS PALSAR-2*
 (b) *Classification result*

Figure 4.2: *Ice classification: blue - open water/very thin ice, cyan - young ice, dark cyan - old ice floes and white - first year ice [from Paper C]*

of the ice cover are indicative of a changing environment. The area/extent of multi year ice, i.e. ice that survived at least two summers, for example is slightly more declining compared to the total ice cover [1].

This thesis focused on the one hand on the discrimination of ice and water, the most basic case of classification, and on the other hand on ice type classification, where only a few visually distinguishable classes have been selected. In both cases multi-spectral comparisons of C- and L-band has been conducted to investigate the possibly complementary information content of the two frequencies. While ice type classification has been applied on L-band data, no studies on distinct ice/water discrimination have been published to the authors knowledge.

The general procedure of ice classification is similar to the one for ice concentration estimation. A set of features separating the ice classes is defined and a mapping technique is applied to link the feature vector to a certain class.

Ice/water maps have been derived from Gray level co-occurrence texture features in conjunction with a Support Vector Machine (SVM) from RADARSAT-2 data [14]. A more complex algorithm fuses the ice-water output of a SVM with an unlabelled six class segmentation to obtain a more robust classification result [71]. While these are algorithms specifically designed for ice/water discrimination, basically any ice classification containing an open water class can be used for this task.

Ice type classification/segmentation is a far wider field and many studies have been conducted in this field addressing different classification tasks [72, 73, 74]. Figure 4.2 shows a classification based on backscatter signatures of an ALOS PALSAR-2 L-band into visually distinguishable ice classes. It visualizes the challenges for a computer algorithm to discriminate different ice regimes, a human can identify.

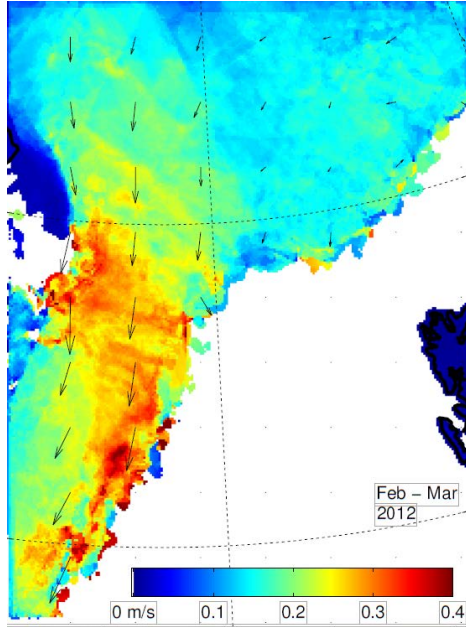


Figure 4.3: *Example of ice drift in Fram Strait [77]*

The potential benefit of multi-frequency SAR imagery has been addressed in the foregoing chapter and comparison studies have revealed a potential benefit of combining them to achieve more accurate classification results [15, 44, 75, 76]. Nevertheless only one study used C- and L-band imagery simultaneously to obtain a combined classification result from satellite SAR data using the ISODATA algorithm on intensity imagery [43]. The challenge of multi-frequency analysis of spaceborne SAR imagery is the availability of near coincidental datasets required due to the constant motion of the ice cover.

4.3 Sea Ice Motion

The sea ice cover is constantly changing in space and time due to the influence of both the atmosphere and ocean. Sea ice drift, the motion of the ice relative to Earth's surface, is forced by geostrophic winds and ocean currents and is quantified by its velocity and direction. Drift velocities up to 0.64 m s^{-1} have been observed in Fram Strait from buoy data [78]. Figure 4.3 shows mean ice velocities estimated from SAR imagery in Fram Strait February to March 2012 [77]. The figure underlines the dynamics in Fram Strait and that the motion of the ice is not negligible when comparing images or auxiliary data acquired at different times.

Motion of the ice is not homogeneous over the area covered within the swath width of an image and is a complex mixture of lateral movement and rotation. The constant motion of the ice creates divergence and shear, resulting in the formation of leads, as well as convergence causing the build up of pressure ridges, that can reach several meters in height [79].

The extraction of sea ice drift from SAR imagery is an active field of research and different algorithms have been proposed [13, 80, 81]. Some studies included L-band data into their investigations [82, 83].

Though sea ice motion is not directly addressed by the research in this study, it imposes challenges on sea ice monitoring and parameter estimation. Whenever comparing data, be it imagery or auxiliary data, acquired at different times, changes due to the drift of the ice need to be kept in mind for the analysis.

5 Summary of Appended Papers

5.1 Paper A: Sea ice concentration estimation from Sentinel-1 Synthetic Aperture Radar images over Fram Strait

In this paper an algorithm for sea ice concentration estimation from Sentinel-1 Synthetic Aperture Radar images is presented and evaluated for Fram Strait, the main gateway to the Arctic. The algorithm is based on spatial autocorrelation, a textural feature which is used on the one hand to distinguish ice and open water and areas of different ice concentration on the other hand. While the backscatter of open water is assumed to fluctuate independently between resolution cells, neighboring pixels exhibit more correlation over a compact ice sheet [52]. In regions with lower ice concentration the autocorrelation is usually lower, as a mixture of ice, open water or sub resolution ice floes is present and lead to a more random backscatter. A generally higher backscatter compared to the open water enables the distinction. Problems remain for fast ice areas which exhibit little structure and have low backscatter values. Dual polarization imagery greatly improves ice/water contrast as the cross-polarization channel is not susceptible to backscatter increases caused by a wind roughened ocean surface.

The mapping between image parameters and ice concentration is performed via an artificial neural network. Neural networks are capable of complex mapping tasks and once trained they can be applied to images of the same kind. Ice concentration charts from the Norwegian Meteorological Institute are used for the necessary training of the network. Generally the algorithm shows a good performance, but improvements are needed for fast ice and some areas in the marginal ice zone, the transition between the open ocean and the compact sea ice.

5.2 Paper B: Comparison of ice/water classification in Fram Strait from C- and L-band SAR imagery

In this paper an algorithm for ice/water classification is evaluated for SAR imagery in C- and L-band and the results of the two different frequencies are compared to each other. The algorithm is based on the one developed in Paper A but has been adapted to the needs of a three class classifier with categories ice, rough open water and calm open water/thin ice. The partition of the water class is necessary as fundamentally different image characteristics are observed. In co-polarization

wind roughened water can basically take any backscatter value, while areas of calm water or where wave dampening occurs, e.g. due to a layer of thin ice or a film of natural organic matter, have a low backscatter due to specular reflection.

The observation area is again Fram Strait because of its pronounced sea ice dynamics and its importance as a gateway to the Arctic. Two different frequencies are used as they respond to distinct features of the ice cover. L-band is more sensitive for topographic features like ridges or floe edges while C-band reacts more to small scale surface roughness and features, i.e. frost flowers. Ground truth for wide swath sea ice imagery is generally difficult and also varies in spatial resolution. Ice extent maps derived from passive microwave radiometry and ice concentration charts from the Norwegian Meteorological Institute are used in this case for evaluation of the algorithm performance. Deviations occurred mostly in the marginal ice zone, where the dynamics of this region exacerbate the difference due to a time lag between the imagery and validation data. Furthermore details get lost by manual interpretation and the larger pixel sizes of the validation data.

The ice/water classification derived from C- and L-band mostly agree but each frequency shows different strengths. C-band is generally better in distinction of ice and water while L-band maps have their strength with open or newly refrozen areas within the ice pack. The first is attributed to the larger contrast between ice and water backscatter especially at cross-polarization while the latter is caused by the larger wavelength of L-band which reduces the susceptibility to small scale surface roughness on the otherwise smooth ice. Deviations occur mostly in the marginal ice zone due to the time lag between the acquisitions and the dynamics at the edge of the ice.

Improvements could be achieved by inclusion of more texture features, which discriminate the classes. Furthermore distinct algorithms for ascending and descending orbital paths could be used, as they exhibit different incidence angle dependences on the backscatter.

5.3 Paper C: Information Content of Multi-Spectral SAR – Sea Ice Classification - Test Case Fram Strait

Paper C investigates the potential benefit of using C- and L-band SAR imagery for sea ice classification in different ice regimes, e.g. pack ice, marginal ice zone and areas with land fast ice. Three examples of dual frequency image pairs have been classified with a Support Vector Machine based on backscatter signatures in co- and cross-polarization channel. One of the example image pairs has been coregistered to see the immediate effect of the combination of two frequencies. This is generally a challenging task for spaceborne observations of sea ice due to the time lag of the images from different sensors. Especially in Fram Strait where the drift can reach several decimetres per second, time gaps of two hours yield significant displacement at the resolution scale of the SAR data. The inhomogeneous and complex motion patterns make correction for ice drift a challenging task.

The investigations reveal that C- and -L-band contain different information that could be exploited for improvement of classification results. Ice floe boundaries

and deformation features are better outlined in L-band, while C-band showed a better separation of ice classes in consolidated pack ice. Different stages of thin and young ice and open water could be better discriminated in C-band while in L-band only thin ice deformation features indicate the difference between thin ice and open water.

Though the results show promising indications of using dual frequency data for more robust and accurate classification results, the time gap between observations impede a quantification of the obtained results.

6 Conclusions and Outlook

The objective of the thesis was the development of strategies for sea ice information retrieval from SAR imagery in C- and L-band of present satellite sensors. The studies presented in the appended papers, included ice concentration estimation, ice/water discrimination and ice type classification. The developed algorithms have been validated against available auxiliary data, i.e ice charts, radiometer data sets or manual derivation of ground. Despite a purposely low number of input features, satisfactory results could be achieved.

The presented work demonstrates the benefit of multi-frequency analysis and the complementary information found in C- and L-band. Furthermore the same algorithm, but tuned to each frequency, can be used without major adaptations. An attempt to co-register detailed images from C- and L-band shows the difficulty of simultaneous use of satellite imagery acquired at different times. In particular, the small scale features like leads and areas with smaller floes or lower ice concentration, which are more sensitive to sea ice motion, are difficult to map adequately.

Though good results can be achieved, future work must focus on further improving the algorithms. There are ice regimes where the performance is still limited. Ice drift estimations obtained from the imagery could be used to account for the motion of the ice in multi-frequency approaches. But this will remain a challenging task as ice motion is complex and highly spatially variant.

We also want to direct our research to ice thickness retrieval from altimeter data (CRYOSAT-2 and Sentinel-3) and investigate how this can possibly be aided by information about ice type or concentration obtained from SAR imagery. Multi year and first year ice are characterized by different ice thickness, with the latter one being thinner than the first one, but also different ice properties. Information about ice type could therefore aid the conversion from sea ice freeboard to thickness. The sea ice concentration on the other hand might alleviate the interpretation of waveforms.

Bibliography

- [1] J. C. Comiso. Large Decadal Decline of the Arctic Multiyear Ice Cover. *Journal of Climate*, **25**(4) (2012), 1176–1193. DOI: [10.1175/jcli-d-11-00113.1](https://doi.org/10.1175/jcli-d-11-00113.1).
- [2] R. Lindsay and A. Schweiger. Arctic sea ice thickness loss determined using subsurface, aircraft, and satellite observations. *The Cryosphere*, **9**(1) (2015), 269–283. DOI: [10.5194/tc-9-269-2015](https://doi.org/10.5194/tc-9-269-2015).
- [3] G. A. Maykut. “The Surface Heat and Mass Balance”. *The Geophysics of Sea Ice*. Ed. by N. Untersteiner. Boston, MA: Springer US, 1986, pp. 395–463. ISBN: 978-1-4899-5352-0. DOI: [10.1007/978-1-4899-5352-0_6](https://doi.org/10.1007/978-1-4899-5352-0_6).
- [4] V. M. Eguiluz, J. Fernández-Gracia, X. Irigoien, and C. M. Duarte. A quantitative assessment of Arctic shipping in 2010–2014. *Scientific Reports*, **6**(1) (2016), 30682. DOI: [10.1038/srep30682](https://doi.org/10.1038/srep30682).
- [5] A. R. Mahoney, J. R. Bockstoce, D. B. Botkin, H. Eicken, and R. A. Nisbet. Sea-Ice Distribution in the Bering and Chukchi Seas: Information from Historical Whaleships’ Logbooks and Journals. *Arctic* (2011), 465–477.
- [6] C. Weyprecht. *Die Metamorphosen des Polareises: Österr.-Ungar. Arktische Expedition 1872-1874*. Perles, 1879.
- [7] F. Nansen, ed. *The Norwegian North Polar Expedition, 1893-1896: Scientific Results*. Longmans, Green and Company, 1904.
- [8] L. Ellsworth and E. H. Smith. Report of the Preliminary Results of the Aeroarctic Expedition with ”Graf Zeppelin,” 1931. *Geographical Review*, **22**(1) (1932), 61–82. DOI: [10.2307/209526](https://doi.org/10.2307/209526).
- [9] W. N. Meier, G. Peng, D. J. Scott, and M. H. Savoie. Verification of a new NOAA/NSIDC passive microwave sea-ice concentration climate record. *Polar Research*, **33**(1) (2014), 21004. DOI: [10.3402/polar.v33.21004](https://doi.org/10.3402/polar.v33.21004).
- [10] W. N. Meier, J. S. Stewart, Y. Liu, J. Key, and J. A. Miller. Operational Implementation of Sea Ice Concentration Estimates From the AMSR2 Sensor. *IEEE Journal of Selected Topics in Applied Earth Observations and Remote Sensing* (2017), 1–8. DOI: [10.1109/jstars.2017.2693120](https://doi.org/10.1109/jstars.2017.2693120).

- [11] Y. Ye, G. Heygster, and M. Shokr. Improving Multiyear Ice Concentration Estimates With Reanalysis Air Temperatures. *IEEE Transactions on Geoscience and Remote Sensing*, **54**(5) (2016), 2602–2614. DOI: [10.1109/tgrs.2015.2503884](https://doi.org/10.1109/tgrs.2015.2503884).
- [12] S. W. Laxon, K. A. Giles, A. L. Ridout, D. J. Wingham, R. Willatt, R. Cullen, R. Kwok, A. Schweiger, J. Zhang, C. Haas, S. Hendricks, R. Krishfield, N. Kurtz, S. Farrell, and M. Davidson. CryoSat-2 estimates of Arctic sea ice thickness and volume. *Geophysical Research Letters*, **40**(4) (2013), 732–737. DOI: [10.1002/grl.50193](https://doi.org/10.1002/grl.50193).
- [13] A. A. Korosov and P. Rampal. A Combination of Feature Tracking and Pattern Matching with Optimal Parametrization for Sea Ice Drift Retrieval from SAR Data. *Remote Sensing*, **9**(3) (2017), 258. ISSN: 2072-4292. DOI: [10.3390/rs9030258](https://doi.org/10.3390/rs9030258).
- [14] N. Zakhvatkina, A. Korosov, S. Muckenhuber, S. Sandven, and M. Babiker. Operational algorithm for ice–water classification on dual-polarized RADARSAT-2 images. *The Cryosphere*, **11**(1) (2017), 33–46. DOI: [10.5194/tc-11-33-2017](https://doi.org/10.5194/tc-11-33-2017).
- [15] A. M. Johansson, J. A. King, A. P. Doulgeris, S. Gerland, S. Singha, G. Spreen, and T. Busche. Combined observations of Arctic sea ice with near-coincident colocated X-band, C-band, and L-band SAR satellite remote sensing and helicopter-borne measurements. *Journal of Geophysical Research: Oceans*, **122**(1) (2017), 669–691. DOI: [10.1002/2016jc012273](https://doi.org/10.1002/2016jc012273).
- [16] F. T. Ulaby, R. K. Moore, and A. K. Fung. *Microwave remote sensing active and passive-volume III: from theory to applications*. Artech House, Inc, 1986.
- [17] B. Rudels, H. J. Friedrich, and D. Quadfasel. The Arctic Circumpolar Boundary Current. *Deep Sea Research Part II: Topical Studies in Oceanography*, **46**(6-7) (1999), 1023–1062. DOI: [10.1016/s0967-0645\(99\)00015-6](https://doi.org/10.1016/s0967-0645(99)00015-6).
- [18] M. Skolnik. *Radar Handbook*. McGraw-Hill Education Ltd, 2008. 1328 pp. ISBN: 0071485473.
- [19] IEEE Standard Letter Designations for Radar-Frequency Bands. *IEEE Std 521-2002 (Revision of IEEE Std 521-1984)* (2003). DOI: [10.1109/IEEESTD.2003.94224](https://doi.org/10.1109/IEEESTD.2003.94224).
- [20] W. G. Rees. *Physical Principles of Remote Sensing*. Cambridge University Press, 2012. DOI: [10.1017/cbo9781139017411](https://doi.org/10.1017/cbo9781139017411).
- [21] R. J. Sullivan. *Radar Foundations for Imaging and Advanced Concepts*. SciTech Publishing, 2004. DOI: [10.1049/sbra030e](https://doi.org/10.1049/sbra030e).
- [22] J. A. Richards. *Remote Sensing with Imaging Radar*. Springer Berlin Heidelberg, 2009. DOI: [10.1007/978-3-642-02020-9](https://doi.org/10.1007/978-3-642-02020-9).

- [23] I. H. Woodhouse. *Introduction to microwave remote sensing*. CRC press, 2005.
- [24] M. A. Richards, J. A. Scheer, and W. A. Holm, eds. *Principles of Modern Radar: Basic principles*. SciTech Publishing, 2010.
- [25] W. C. Carrara, R. M. Majewski, and R. S. Goodman. *Spotlight Synthetic Aperture Radar: Signal Processing Algorithms*. Artech House, Inc, 1995. 572 pp. ISBN: 0890067287.
- [26] I. G. Cumming and F. H. Wong. *Digital processing of synthetic aperture radar data*. Artech House, Inc, 2005.
- [27] A. Currie and M. Brown. Wide-swath SAR. *IEE Proceedings F Radar and Signal Processing*, **139**(2) (1992), 122–135. DOI: 10.1049/ip-f-2.1992.0016.
- [28] F. D. Zan and A. M. Guarnieri. TOPSAR: Terrain Observation by Progressive Scans. *IEEE Transactions on Geoscience and Remote Sensing*, **44**(9) (2006), 2352–2360. DOI: 10.1109/tgrs.2006.873853.
- [29] P. Prats-Iraola, R. Scheiber, M. Rodriguez-Cassola, J. Mittermayer, S. Wollstadt, F. D. Zan, B. Brautigam, M. Schwerdt, A. Reigber, and A. Moreira. On the Processing of Very High Resolution Spaceborne SAR Data. *IEEE Transactions on Geoscience and Remote Sensing*, **52**(10) (2014), 6003–6016. DOI: 10.1109/tgrs.2013.2294353.
- [30] F. T. Ulaby, R. K. Moore, and A. K. Fung. *Microwave Remote Sensing Active and Passive- Volume II: Radar Remote Sensing and Surface Scattering and Emission Theory*. Addison-Wesley Publishing Company, Inc., 1982.
- [31] N. S. Mohammed Shokr. *Sea Ice: Physics and Remote Sensing*. American Geophysical Union, 2015. 600 pp. ISBN: 1119027896.
- [32] I. S. Robinson. *Measuring the Oceans from Space*. Springer-Verlag GmbH, 2004. ISBN: 3540426477.
- [33] F. T. Ulaby and D. G. Long. *Microwave Radar and Radiometric Remote Sensing*. The University of Michigan Press, 2013. 1116 pp. ISBN: 0472119354.
- [34] P. W. Vachon and J. Wolfe. C-Band Cross-Polarization Wind Speed Retrieval. *IEEE Geoscience and Remote Sensing Letters*, **8**(3) (2011), 456–459. DOI: 10.1109/lgrs.2010.2085417.
- [35] B. Scheuchl, D. Flett, R. Caves, and I. Cumming. Potential of RADARSAT-2 data for operational sea ice monitoring. *Canadian Journal of Remote Sensing*, **30**(3) (2004), 448–461. DOI: 10.5589/m04-011. eprint: <http://dx.doi.org/10.5589/m04-011>.
- [36] M. Gade, W. Alpers, H. Hühnerfuss, V. R. Wissmann, and P. A. Lange. On the Reduction of the Radar Backscatter by Oceanic Surface Films. *Remote*

Sensing of Environment, **66**(1) (1998), 52–70. DOI: 10.1016/s0034-4257(98)00034-0.

- [37] P. Clemente-Colón and X.-H. Yan. Low-backscatter ocean features in synthetic aperture radar imagery. *Johns Hopkins APL Technical Digest*, **21**(1) (2000), 116–121.
- [38] F. D. Carsey, ed. *Microwave remote sensing of sea ice*. American Geophysical Union, 1992.
- [39] L. Kaleschke and G. Heygster. Towards multi-sensor microwave remote sensing of frost flowers on sea ice. *Annals of Glaciology*, **39**(1) (2004), 219–222.
- [40] L. M. H. Ulander, A. Carlström, and J. Askne. Effect of frost flowers, rough saline snow and slush on the ERS-1 SAR backscatter of thin Arctic sea-ice. *International Journal of Remote Sensing*, **16**(17) (1995), 3287–3305. DOI: 10.1080/01431169508954631.
- [41] A. Carlström and L. M. H. Ulander. Validation of backscatter models for level and deformed sea-ice in ERS-1 SAR images. *International Journal of Remote Sensing*, **16**(17) (1995), 3245–3266. DOI: 10.1080/01431169508954629.
- [42] A. Carlström and L. M. H. Ulander. C-band backscatter signatures of old sea ice in the central Arctic during freeze-up. *IEEE Transactions on Geoscience and Remote Sensing*, **31**(4) (1993), 819–829. DOI: 10.1109/36.239904.
- [43] W. Dierking and T. Busche. Sea ice monitoring by L-band SAR: an assessment based on literature and comparisons of JERS-1 and ERS-1 imagery. *IEEE Transactions on Geoscience and Remote Sensing*, **44**(4) (2006), 957–970. DOI: 10.1109/tgrs.2005.861745.
- [44] L. E. Eriksson, K. Borenäs, W. Dierking, A. Berg, M. Santoro, P. Pemberton, H. Lindh, and B. Karlson. Evaluation of new spaceborne SAR sensors for sea-ice monitoring in the Baltic Sea. *Canadian Journal of Remote Sensing*, **36**(S1) (2010), S56–S73. DOI: 10.5589/m10-020.
- [45] M. Mäkinen and M. Hallikainen. Investigation of C- and X-band backscattering signatures of Baltic Sea ice. *International Journal of Remote Sensing*, **25**(11) (2004), 2061–2086. DOI: 10.1080/01431160310001647697.
- [46] W. Dierking and J. Dall. Sea-Ice Deformation State From Synthetic Aperture Radar Imagery—Part I: Comparison of C- and L-Band and Different Polarization. *IEEE Transactions on Geoscience and Remote Sensing*, **45**(11) (2007), 3610–3622. DOI: 10.1109/tgrs.2007.903711.
- [47] J. Karvonen. Baltic Sea Ice Concentration Estimation Based on C-Band Dual-Polarized SAR Data. *IEEE Transactions on Geoscience and Remote Sensing*, **52**(9) (2014), 5558–5566. DOI: 10.1109/tgrs.2013.2290331.

- [48] R. M. Haralick, K. Shanmugam, and I. Dinstein. Textural Features for Image Classification. *IEEE Transactions on Systems, Man, and Cybernetics*, **SMC-3**(6) (1973), 610–621. DOI: 10.1109/tsmc.1973.4309314.
- [49] D. A. Clausi. An analysis of co-occurrence texture statistics as a function of grey level quantization. *Canadian Journal of Remote Sensing*, **28**(1) (2002), 45–62. DOI: 10.5589/m02-004. eprint: <http://dx.doi.org/10.5589/m02-004>.
- [50] L.-K. Soh and C. Tsatsoulis. Texture analysis of SAR sea ice imagery using gray level co-occurrence matrices. *IEEE Transactions on Geoscience and Remote Sensing*, **37**(2) (1999), 780–795. DOI: 10.1109/36.752194.
- [51] J. Karvonen. Baltic Sea Ice Concentration Estimation Based on C-Band HH-Polarized SAR Data. *IEEE Journal of Selected Topics in Applied Earth Observations and Remote Sensing*, **5**(6) (2012), 1874–1884. DOI: 10.1109/jstars.2012.2209199.
- [52] A. Berg and L. E. B. Eriksson. SAR Algorithm for Sea Ice Concentration—Evaluation for the Baltic Sea. *IEEE Geoscience and Remote Sensing Letters*, **9**(5) (2017), 938–942. DOI: 10.1109/lgrs.2012.2186280.
- [53] H. Deng and D. Clausi. Unsupervised segmentation of synthetic aperture Radar sea ice imagery using a novel Markov random field model. *IEEE Transactions on Geoscience and Remote Sensing*, **43**(3) (2005), 528–538. DOI: 10.1109/tgrs.2004.839589.
- [54] M. Haidekker. “Texture Analysis”. *Advanced Biomedical Image Analysis*. John Wiley & Sons, Inc., 2010, pp. 236–275. DOI: 10.1002/9780470872093.ch8.
- [55] T. Geldsetzer, M. Arkett, T. Zagon, F. Charbonneau, J. J. Yackel, and R. K. Scharien. All-Season Compact-Polarimetry C-band SAR Observations of Sea Ice. *Canadian Journal of Remote Sensing*, **41**(5) (2015), 485–504. DOI: 10.1080/07038992.2015.1120661.
- [56] T. Eltoft, J. Grahn, A. Doulgeris, C. Brekke, L. Ferro-Famil, and B. Holt. Multi-frequency polarimetric analysis of sea ice. *Conference Proceedings of 2013 Asia-Pacific Conference on Synthetic Aperture Radar (APSAR)*. 2013, pp. 96–99.
- [57] J. A. Casey, S. E. Howell, A. Tivy, and C. Haas. Separability of sea ice types from wide swath C- and L-band synthetic aperture radar imagery acquired during the melt season. *Remote Sensing of Environment*, **174** (2016), 314–328. DOI: 10.1016/j.rse.2015.12.021.
- [58] K. C. Partington, J. D. Flach, D. Barber, D. Isleifson, P. J. Meadows, and P. Verlaan. Dual-Polarization C-Band Radar Observations of Sea Ice in the Amundsen Gulf. *IEEE Transactions on Geoscience and Remote Sensing*, **48**(6) (2010), 2685–2691. DOI: 10.1109/tgrs.2009.2039577.

- [59] *Radarsat-2 Product Description*. MacDonald, Dettweiler and Associates Ltd., 2016.
- [60] T. Vihma. Effects of Arctic sea ice decline on weather and climate: a review. *Surveys in Geophysics*, **35**(5) (2014), 1175–1214. DOI: [10.1007/s10712-014-9284-0](https://doi.org/10.1007/s10712-014-9284-0).
- [61] L. Pizzolato, S. E. L. Howell, J. Dawson, F. Laliberté, and L. Copland. The influence of declining sea ice on shipping activity in the Canadian Arctic. *Geophysical Research Letters*, **43**(23) (2016), 12, 146–12, 154. DOI: [10.1002/2016gl071489](https://doi.org/10.1002/2016gl071489).
- [62] JCOMM Expert Team on Sea Ice. *WMO Sea-Ice Nomenclature, volumes I, II and III*. WMO, 2015.
- [63] D. J. Cavalieri, C. L. Parkinson, P. Gloersen, and H. J. Zwally. *Sea Ice Concentrations from Nimbus-7 SMMR and DMSP SSM/I-SSMIS Passive Microwave Data, Version 1*. NASA National Snow and Ice Data Center Distributed Active Archive Center, 1996, yearly updated.
- [64] G. Spreen, L. Kaleschke, and G. Heygster. Sea ice remote sensing using AMSR-E 89-GHz channels. *Journal of Geophysical Research*, **113**(C2) (2008). DOI: [10.1029/2005jc003384](https://doi.org/10.1029/2005jc003384).
- [65] World Metrological Organization. *Sea-Ice Information Services in the World*. World Metrological Institution, 2010.
- [66] J. Karvonen, J. Vainio, M. Marnela, P. Eriksson, and T. Niskanen. A Comparison Between High-Resolution EO-Based and Ice Analyst-Assigned Sea Ice Concentrations. *IEEE Journal of Selected Topics in Applied Earth Observations and Remote Sensing*, **8**(4) (2015), 1799–1807. DOI: [10.1109/jstars.2015.2426414](https://doi.org/10.1109/jstars.2015.2426414).
- [67] F. Fleuret, T. Li, C. Dubout, E. K. Wampler, S. Yantis, and D. Geman. Comparing machines and humans on a visual categorization test. *Proceedings of the National Academy of Sciences*, **108**(43) (2011), 17621–17625. DOI: [10.1073/pnas.1109168108](https://doi.org/10.1073/pnas.1109168108).
- [68] N. G. Kasapoglu. Sea Ice Concentration Retrieval Using Composite ScanSAR Features in a SAR Data Assimilation Process. *IEEE Geoscience and Remote Sensing Letters*, **11**(12) (2014), 2085–2089. DOI: [10.1109/lgrs.2014.2319212](https://doi.org/10.1109/lgrs.2014.2319212).
- [69] L. Wang, K. A. Scott, L. Xu, and D. A. Clausi. Sea Ice Concentration Estimation During Melt From Dual-Pol SAR Scenes Using Deep Convolutional Neural Networks: A Case Study. *IEEE Transactions on Geoscience and Remote Sensing*, **54**(8) (2016), 4524–4533. DOI: [10.1109/tgrs.2016.2543660](https://doi.org/10.1109/tgrs.2016.2543660).
- [70] H. Wakabayashi and S. Sakai. Estimation of sea ice concentration in the Sea of Okhotsk using PALSAR polarimetric data. *2010 IEEE International*

Geoscience and Remote Sensing Symposium. IEEE, 2010. doi: 10.1109/igarss.2010.5652440.

- [71] S. Leigh, Z. Wang, and D. A. Clausi. Automated Ice–Water Classification Using Dual Polarization SAR Satellite Imagery. *IEEE Transactions on Geoscience and Remote Sensing*, **52**(9) (2014), 5529–5539. doi: 10.1109/tgrs.2013.2290231.
- [72] D. Clausi, A. Qin, M. Chowdhury, P. Yu, and P. Maillard. MAGIC: MAP-guided ice classification system. *Canadian Journal of Remote Sensing*, **36**(S1) (2010), S13–S25.
- [73] T.-J. Kwon, J. Li, and A. Wong. ETVOS: An Enhanced Total Variation Optimization Segmentation Approach for SAR Sea-Ice Image Segmentation. *IEEE Transactions on Geoscience and Remote Sensing*, **51**(2) (2013), 925–934. doi: 10.1109/tgrs.2012.2205259.
- [74] M.-A. N. Moen, A. P. Doulgeris, S. N. Anfinsen, A. H. H. Renner, N. Hughes, S. Gerland, and T. Eltoft. Comparison of feature based segmentation of full polarimetric SAR satellite sea ice images with manually drawn ice charts. *The Cryosphere*, **7**(6) (2013), 1693–1705. doi: 10.5194/tc-7-1693-2013.
- [75] R. Ressel and S. Singha. Comparing Near Coincident Space Borne C and X Band Fully Polarimetric SAR Data for Arctic Sea Ice Classification. *Remote Sensing*, **8**(3) (2016), 198. doi: 10.3390/rs8030198.
- [76] W. Dierking. Sea ice classification on different spatial scales for operational and scientific use. *ESA Living Planet Symposium 2013*. (Edinburgh). 2013.
- [77] A. Berg. “Spaceborne synthetic aperture radar for sea ice observations, concentration and dynamics”. PhD thesis. Chalmers University of Technology, 2014.
- [78] R. Lei, P. Heil, J. Wang, Z. Zhang, Q. Li, and N. Li. Characterization of sea-ice kinematic in the Arctic outflow region using buoy data. *Polar Research*, **35**(1) (2016), 22658.
- [79] M. Leppäranta. *The Drift of Sea Ice*. Springer-Verlag GmbH, 2011. ISBN: 3642046827.
- [80] S. Muckenhuber and S. Sandven. Open-source sea ice drift algorithm for Sentinel-1 SAR imagery using a combination of feature tracking and pattern matching. *The Cryosphere*, **11**(4) (2017), 1835–1850. doi: 10.5194/tc-11-1835-2017.
- [81] A. Berg and L. E. B. Eriksson. Investigation of a Hybrid Algorithm for Sea Ice Drift Measurements Using Synthetic Aperture Radar Images. *IEEE Transactions on Geoscience and Remote Sensing*, **52**(8) (2014), 5023–5033. doi: 10.1109/tgrs.2013.2286500.

- [82] A. M. Johansson and A. Berg. Agreement and Complementarity of Sea Ice Drift Products. *IEEE Journal of Selected Topics in Applied Earth Observations and Remote Sensing*, **9**(1) (2016), 369–380. doi: [10.1109/jstars.2015.2506786](https://doi.org/10.1109/jstars.2015.2506786).
- [83] J. Lehtiranta, S. Siiriä, and J. Karvonen. Comparing C- and L-band SAR images for sea ice motion estimation. *The Cryosphere*, **9**(1) (2015), 357–366. doi: [10.5194/tc-9-357-2015](https://doi.org/10.5194/tc-9-357-2015).